Femtosecond transmission electron microscopy for nanoscale photonics: a numerical study

C. W. Barlow Myers, N. J. Pine and W. A. Bryan (w.a.bryan@swansea.ac.uk)

Department of Physics, College of Science, Swansea University,

Singleton Park, Swansea SA2 8PP, UK

Supplementary information

S1: Electron source

The modelled ultrafast electron source is presented in figure S1, with the static electric field around the NSMT and suppressor shown in figure S1(a). The saddle induced by the suppressor is indicated by thick magenta lines, and the 2σ outer trajectory of the electron pulse is shown in blue. Figure S1(b) is a magnification of the apex of the NSMT, and in (a) and (b), V_{sup} = 70.1 kV and V_{tip} = 70 kV, and the contour lines are separated by 10 V.

We apply a 25 μm fillet to the inner circumference of the suppressor to prevent high field gradients causing field emission, and the maximum surface fields on all electrodes are below 5 MV/m. The nanotip (V_{tip}) and suppressor potentials (V_{sup}) define the field at the emission site. The dominant gradient lies along the z-axis towards the anode and the on-axis field $E_z(z)$ is explored as a function of ΔV, shown in figure S1(c) & (d). Increasing ΔV moves the saddle point towards the apex of the tip and ultimately into the $z \geq 0$ region. This field reversal extinguishes emission, present in figure S1(c) & (d) for $\Delta V > 400$ V.

Changing ΔV modifies the electrostatic landscape around the NSMT, facilitating adjustment of the spatio-temporal distribution of the electron pulses [43]. Reducing the DC field decreases the longitudinal momentum acquired during acceleration (see figure S1(c) & (d)), increasing the total flight time, which increases temporal broadening. Reducing the DC field reduces the transverse momentum and hence reduces the path length differences experienced between the apex and the anode. These processes cannot be varied independently. With V_{tip} = -70 kV, V_{sup} would be set such

that the surface field of the NSMT does not exceed 1.5 GV/m, hence optical field enhancement would only permit electron tunnelling during the presence of the driving laser pulse.

The region between the NSMT and the anode is shown in figure S1(e). The inclusion of a magnetic lens allows divergence to be controlled independently of ΔV. This lens focusses the electron pulse at the aperture of the anode, ensuring distortions induced by fringing fields are minimal, and that all photoemitted flux is used for image generation. Geometric temporal expansion of the pulse is also minimized by reducing path length differences. For a potential difference of 70 kV, a final velocity of 0.48c is anticipated.

Pulse rotation about the z-axis induced by a magnetic lens is proportional to the longitudinal velocity, therefore in the acceleration region, focusing is coupled to the DC field gradient. The best performance (minimal spatial distortion at the anode, and shortest flight time) is found when the pulse has reached a significant proportion of its final velocity, shown through comparison of figures S1(e) and (f), which shows the average longitudinal velocity of the electron pulse. For a final energy of 70 keV, a maximum transverse radius of $2\sigma(r) = 55$ μm is reached, where σ is the standard deviation of the parameter in parenthesis. The optimal balance between minimized $2\sigma(r)$ and a small temporal (geometric) stretch is when a strong magnetic field is applied in the first few millimetres of flight. The convergence angle of 2.5 mrad is at least an order of magnitude smaller than the divergence angle with no magnetic field present.

Comparing figures S1(c) and S1(f) at $z < 10$ nm, the DC field is relatively constant over the first ten nanometres, causing near-constant acceleration. Between 10 nm < z < 100 μm, the electric field transitions between being governed by the NSMT to the parallel plate case, shown in figure S1(d) by the tendency to converge to a constant value at z > 100 μm. The flatness of the contours in figure S1(a) around $z > 100$ μm, the linearity of the electric field E_z in figure S1(d) and the linear increase of velocity with z position in figure S1(f) indicates the completion of the transition between NSMT-influenced acceleration and parallel plate acceleration. Upon exit of the anode the electrons reach their final velocity of $v_z \approx 0.48c$ ($\lambda_e \approx 4.5$ pm).

The total flight time of the electron pulse from the NSMT to the anode is shown in figure S1(g). The significant DC field gradient at the apex causes dramatic acceleration in the first 10 nm, which is a key consideration when trying to mitigate the influence of space charge. The transitional behaviour detailed above is also apparent from the flight time.

S2: Condenser-Objective lens current

The condenser-objective lens currents used for the calculation of figure 5 are shown in figure S2 for parallel and anti-parallel cases.

S3: Energy-time phase space distributions

The key consideration of the THz compressor is that it changes the energy-time phase space occupied by the electron pulse. Pre-compression, the energy bandwidth is dominated by the emission process at the NSMT and the time is dominated by space charge broadening. The THz resonator acts to broaden the bandwidth present in the pulse, with the momentum imparted in such a fashion so as to minimize the temporal duration at the longitudinal focus. To better illustrate the effects of space charge on pulse length compression, in figure S3, the energy-time phase space distributions are shown just before the THz compressor, on the exit of the compressor and at the sample plane, i.e the temporal focus.

As is apparent from figure S3(a) and (b), as the pulse charge increases from one to ten electrons, the duration increase at the compressor means that the pulse picks up the same energy-time chirp gradient over a longer time, hence larger bandwidth. Figure S3(c) illustrates the major issue with compressing 100e pulses, that being the space charge distortion before the compressor causes a non-linear variation of energy with time, limiting the minimum duration achievable by applying only a linear chirp.

S4: Implementation of modelled instrument

The realisation of the modelled fs-TEM architecture will be challenging, and is anticipated to require the modification of elements of TEM technology and integration with novel developments. The

requirement for multiple points of laser access suggests a horizontal rather than vertical electron beampath may be favourable, and that mechanical stability of the electron optics would be improved by directly coupling to the optical table via the vacuum enclosure.

The electrostatics of the electron source region is relatively straightforward, however creating a sufficiently strong magnetic field to facilitate focusing at the anode is non-trivial. Rather than rely on traditional coils, it is suggested that rare earth permanent magnets could be employed, possibly with tuning coils to facilitate variations in the beam energy and steering. Photoemission from the NSMT requires in-vacuum short focal length optics, and the use of permanent magnetic fields may reduce limitations to the geometry around the source region.

The most challenging aspect of the studied instrument is the generation of THz radiation which is reproducible and extremely stable. We anticipate the increased stability of ultrafast lasers and their pump systems will have a beneficial influence on this aspect, and that the adoption of fibre laser technology will be similarly disruptive. Active stabilisation of the pump lasers, ultrafast pulse generation and rectification stages is expected to be vital.

The placement of and access to the THz resonator will be vital, hence the strength of C2 should be set such that a small focus is formed outside the body of the lens to give sufficient room for the resonator and associated nano-positioner. The focusing optic and vacuum window placement will also impact the configuration of this region, and an exit path for the THz radiation would be a valuable diagnostic.

Sample access is likely to be complicated by similar requirements, with the addition of being immersed in the field of the CO lens. A pump laser entrance and exit path, along with optical focusing and diagnostics will need to be located in the vicinity of the sample, albeit with less stringent requirements for a very small spot and high stability as compared to the NSMT illumination. The placement of an additional THz resonator for streaking at the sample plane would also be beneficial, however it may be possible to make use of the path of the pump laser path and optics. Furthermore, an ultrafast IR-pumped electronic or field-enhancement process might be a better alternative as the temporal response of a THz resonator to a 10 fs electron pulse might not produce sufficient streaking.

The stability of electron generation will be primarily governed by laser pointing and pulse energy fluctuations, assuming that the NSMT position is not disrupted by vibration. Minimizing the fluctuation of the number of electrons per pulse is equivalent to controlling the duration at the sample. RMS laser pulse energies of 0.5% over days are reported by manufacturers, and micro-radian pointing or sub-micron positional uncertainties are common with active stabilization, which coupled to optics with focal lengths around 10 cm correspond to intensity fluctuations around 0.3%. If nonlinear optical processes such as optical parametric amplification or frequency doubling are used, such fluctuations could also change the spectrum and duration of the IR drive laser on the NSMT. Electron transport from the source to sample will be governed by the stability of the accelerating voltage and magnetic lens currents. Power supplies have been developed to satisfy stringent requirements in TEM, and are available with part per million stabilities. Overall, the mechanical and thermal stability of electron and optical elements will require the diligence applied to TEMs.

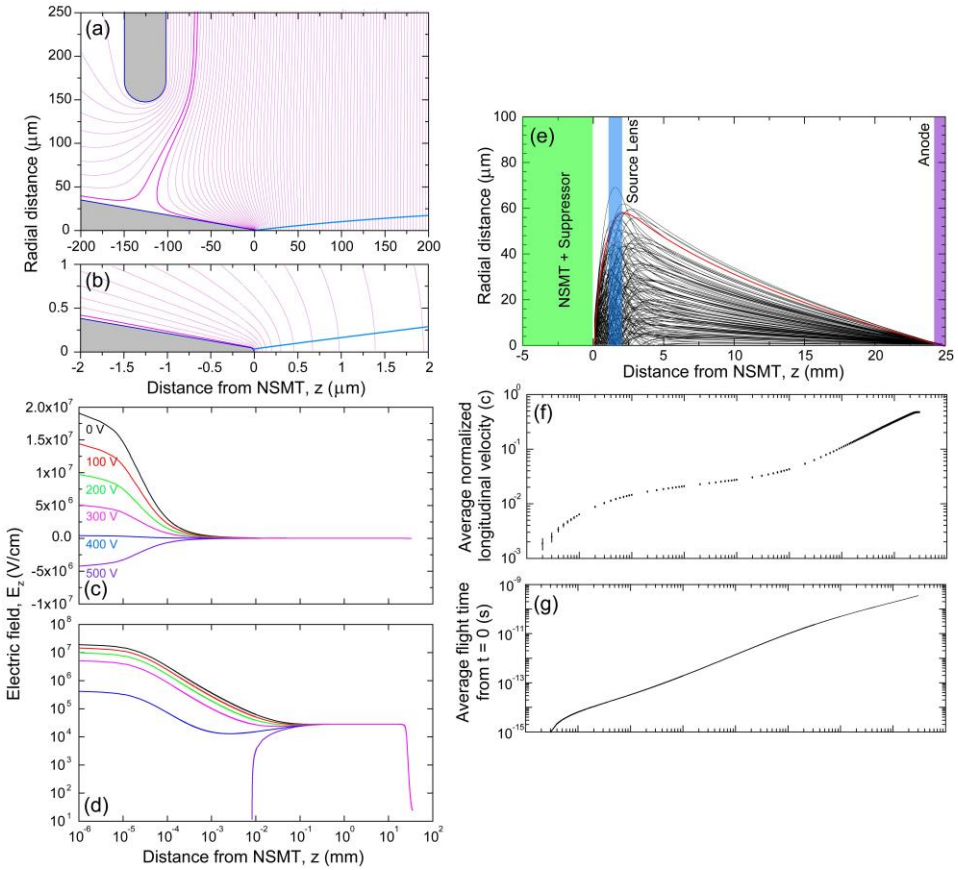

Figure S1. (a) Contour plot of the static (DC) electric field in the vicinity of the NSMT and the suppressor parallel (z-axis) and perpendicular (r-axis) to the axis of cylindrical symmetry. (b) Expanded view of the apex of the NSMT. (c) DC electric field along the z-axis (E_z) induced between combination of the NSMT (at potential V_{tip} = -70 kV) and suppressor (at V_{sup}) and the grounded anode at 25 cm as $\Delta V = V_{tip} - V_{sup}$ is varied between 0 and 500 V, shown on a linear scale. (d) as (c) with $E_z(z)$ on a logarithmic scale. (e) Individual simulation macroparticle trajectories from the NSMT and Suppressor, through the maximum field of the source magnetic lens (blue) and exiting through an aperture (radius 1 mm with 0.5 mm fillet) in the grounded anode (purple). The red line indicates 2σ of the position coordinates of all macroparticles. (f) Longitudinal velocity of the electron pulse averaged over all GPT macroparticles as a function of average *z* position on a logarithmic scale. (g) Average time of flight from creation at time t = 0 as a function of average z position.

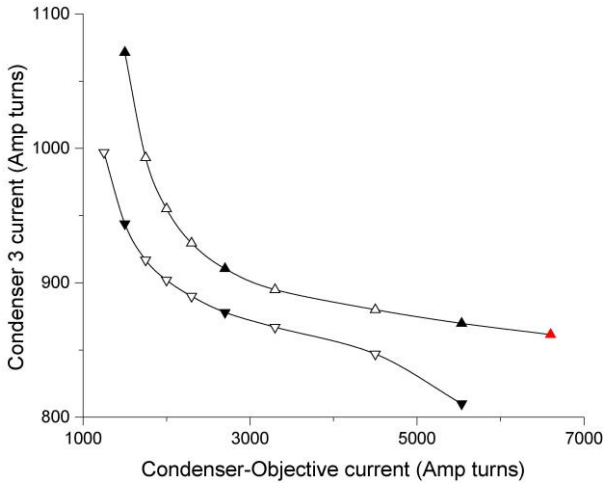

Figure S2. Condenser-objective and lens C3 currents for parallel (up triangles) and anti-parallel (down triangles) current alignments for the results presented in figure 5. The black filled triangles identify the thick lines in figure 5, and the red filled triangle is the smallest electron beam diameter achieved.

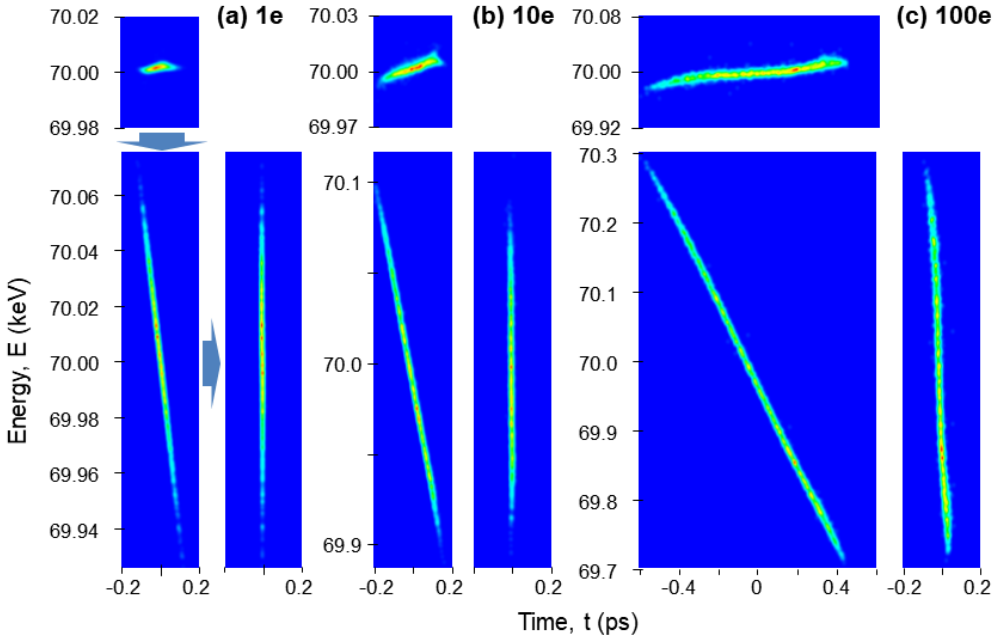

Figure S3. Energy-time phase space distributions for (a) one electron, (b) ten electrons and (c) one hundred electrons. In each case the upper panel is immediately before the entrance to the THz resonator, then the diagonal distribution indicates the action of the resonator, followed by propagation to the longitudinal focus at z = 0.243 m. Note the changing energy scale from (a)-(c), and in all cases the compressor field is 5 MV/m.